NIH Public Access
Author Manuscript
J Biomech. Author manuscript; available in PMC 2014 January 18.

Published in final edited form as:
J Biomech. 2013 January 18; 46(2): 253–265. doi:10.1016/j.jbiomech.2012.10.025.

A review of recent advances in the assessment of bone porosity, permeability, and interstitial fluid flow

Luis Cardoso, **Susannah P. Fritton**, **Gaffar Gailani***, **Mohammed Benalla**, and **Stephen C. Cowin**
Department of Biomedical Engineering The City College of New York New York, NY 10031, U.S.A.

Abstract

This contribution reviews recent research performed to assess the porosity and permeability of bone tissue with the objective of understanding interstitial fluid movement. Bone tissue mechanotransduction is considered to occur due to the passage of interstitial pore fluid adjacent to dendritic cell structures in the lacunar-canalicular porosity. The movement of interstitial fluid is also necessary for the nutrition of osteocytes. This review will focus on four topics related to improved assessment of bone interstitial fluid flow. First, the advantages and limitations of imaging technologies to visualize bone porosities and architecture at several length scales are summarized. Second, recent efforts to measure the vascular porosity and lacunar-canalicular microarchitecture are discussed. Third, studies associated with the measurement and estimation of the fluid pressure and permeability in the vascular and lacunar-canalicular domains are summarized. Fourth, the development of recent models to represent the interchange of fluids between the bone porosities is described.

Keywords

Bone porosity; permeability; interstitial fluid flow; lacunar canalicular system; vascular system

INTRODUCTION: BONE INTERSTITIAL FLUID FLOW

Bone tissue contains two types of fluid, blood and interstitial fluid. Through the arterial system blood arrives containing oxygen and nutrients; after passing through the bone capillaries the blood components then depart containing less oxygen and nutrients, and more carbon dioxide and other cellular waste products. Many substances, including amino acids, sugars, fatty acids, coenzymes, hormones, neurotransmitters, and inorganic compounds, are exchanged from the capillaries into the interstitial fluid in the vascular porosity in cortical bone. The vascular porosity (VP) is the space inside the Haversian and Volkmann canals that contains the soft tissue structures, blood vessels and nerves. The mineralized tissue matrix in bone contains lacunar pores and slender canalicular channels, forming a complex network that is called the lacunar-canalicular porosity (LCP). Lacunar pores are occupied by

© 2012 Elsevier Ltd. All rights reserved

*Department of Mechanical Engineering Technology and Industrial Design New York City College of Technology Brooklyn, NY 11201, U.S.A.

Publisher's Disclaimer: This is a PDF file of an unedited manuscript that has been accepted for publication. As a service to our customers we are providing this early version of the manuscript. The manuscript will undergo copyediting, typesetting, and review of the resulting proof before it is published in its final citable form. Please note that during the production process errors may be discovered which could affect the content, and all legal disclaimers that apply to the journal pertain.

CONFLICT OF INTEREST STATEMENT None

NIH-PA Author Manuscript
NIH-PA Author Manuscript
NIH-PA Author Manuscript

NIH-PA Author Manuscript

NIH-PA Author Manuscript

NIH-PA Author Manuscript

osteocytes, the most abundant cell type in bone, and the canaliculi contain the cell processes emanating from contiguous osteocytes, thus permitting communication between neighboring bone cells. Piekarski and Munro (1977) first proposed that interstitial fluid flow in the lacunar-canalicular system is enhanced by everyday mechanical loading of bone, increasing the transport of nutrients and metabolic waste between the vascular porosity and the lacunar-canalicular porosity. *In situ* measurement of solute transport in the bone lacunar-canalicular system has provided direct evidence for load-induced fluid flow in real-time within the lacunar-canalicular system (Knothe Tate et al. 1998b, Gardinier et al. 2010, Price et al. 2011).

Osteocytes are considered to be the sensors of mechanical strain, in charge of producing the biochemical signals to orchestrate the absorption and/or formation of bone by osteoclasts and osteoblasts, respectively (Cowin et al. 1991, Weinbaum et al. 1994, Burger et al. 1995). An amplification of the mineralized tissue strain levels is proposed to occur when interstitial fluid flow is enhanced by the time-varying mechanical loads applied to bone, causing deformations that result in convection of interstitial fluid in and out of the LCP (Weinbaum et al. 1994, You et al. 2001). The interstitial fluid in the LCP travels inside the canaliculi and lacunae, passing through the space between the osteocyte dendritic process and the canalicular wall, dragging the osteocyte's cell process and deflecting the tethering elements that attach the cell process to the canalicular wall (Wang et al. 2007, McNamara et al. 2009). Focal adhesion complexes and integrins (McNamara et al. 2009) located at the cell process membrane are stretched out, which may lead to the genesis of molecules involved in signaling pathways (e.g., OPG, RANKL, NO, PGE2, ATP, sclerostin, DMP1, FGF23) (Zhou et al. 2008). A review of interstitial fluid flow and mechanotransduction in bone was recently presented by Fritton and Weinbaum (2009).

Theoretical, experimental, and technological developments in recent years have allowed improved characterization of the vascular and lacunar-canalicular system toward better understanding interstitial fluid flow and bone mechanotransduction. This review focuses on research developments documenting the porosity and permeability of bone tissue with the objective of understanding interstitial fluid movement. This review describes efforts to measure the vascular and lacunar-canalicular porosities in bone, as well as the microarchitecture of the osteocyte lacunae and canaliculi, using recently developed imaging technologies. Studies associated with the measurement and estimation of the fluid pressure and permeability in the vascular and lacunar-canalicular domains are summarized, and recent developments of models to represent the interchange of fluid between these two porosities are described.

BONE NESTED POROSITIES

There are three levels of porosity in bone, which are nested hierarchically one inside another as a set of Russian dolls in microcirculatory pathways (Cowin et al. 2009). The largest pore size is associated with the vascular porosity (VP), which consists of the volume of all the tunnels in bone that contain blood vessels and includes all the osteonal canals (primary and secondary) as well as transverse (Volkmann) canals. The lacunar-canalicular porosity (LCP) contains the second largest pore size, and it is associated with the osteocyte lacunae and canaliculi channels. The space between the osteocyte and the lacunar-canalicular wall is filled by the osteocyte's glycocalyx and interstitial fluid. The smallest pore size in bone is found in the collagen-apatite porosity (CAP). The pores are spaced between the collagen and the crystallites of the mineral apatite. At this level, most of the water is bound to ionic crystals in bone (Neuman et al. 1953; Wehrli and Fernandez-Seara 2005). The typical lineal dimension associated with the vascular, lacunar-canalicular, and collagen-apatite porosities is 50 μm, 100 nm, and 1 nm, respectively (Cowin 1999).

NIH-PA Author Manuscript

NIH-PA Author Manuscript

NIH-PA Author Manuscript

IMAGING OF BONE

Light microscopy (LM) has been one of the most widely used imaging technologies to characterize bone microarchitecture. Video microscopy images taken with video recorders were used some decades ago to acquire gross images of bone cross sections to assess vascular porosity. This technology was the precursor of current microscope digital cameras, which combined with enhanced optics allow automated acquisition of a sequence of images at different focal points to create 3D renderings from histological sections. This approach is well adapted for decalcified and soft tissue, but is limited by the low penetration of photons in calcified tissue. With the development of confocal laser scanning microscopy (CLSM), the 3D characterization of the vascular and lacunar-canalicular network was substantially improved. CLSM uses a point source illumination and pinhole detection to eliminate light outside of the focal plane. The imaging capabilities of both LM and CLSM are in general restricted by the optical resolution limit (~200 nm in the focal plane). Thus, confocal microscopy can overestimate canalicular measurements due to partial volume effects (Sharma et al. 2012). However, this resolution is appropriate for architectural measurements of lacunae. A second limitation of CLSM is the optical distortion due to the large mismatch in refraction index between the immersion oil and the high density of bone tissue, which creates depth-dependent geometrical distortions in 3D confocal image stacks. While LM and CLSM can provide detailed assessment of bone microarchitecture, the histological processing required for these imaging modalities, the low penetration depth, and the errors arising from 2D mechanical sectioning are among the inconveniences of these approaches. New interference approaches, non-linear imaging, and super-resolution microscopes may achieve imaging below the optical limit, ~20 nm (Garini et al. 2005, Hell 2007, Heintzmann and Ficz 2006).

The development of microradiography, micro- and nano-computed tomography (μCT, nanoCT), transmission X-ray microscopy CT (TXM CT), and synchrotron radiation micro-computed tomography (SR-μCT) have opened a myriad of possibilities to investigate bone microarchitecture. In contrast to photons, X-rays can penetrate dense materials such as bone, and most of these approaches produce true 3D representations of the vascular and lacunar porosities. Laboratory desktop μCT and nanoCT systems can achieve micron and submicron resolution images, respectively (Table 1). In general, they can image relatively large volumes of interest, and they have sufficient resolution to characterize the vascular and lacunar porosities, but not the canalicular channels. SR-μCT can achieve resolutions up to 50 nm, with better contrast than laboratory-based μCT and nanoCT since the former uses a monochromatic synchrotron X-ray light source, and the latter uses a non-coherent laboratory X-ray point source. However, there is a trade-off between resolution and volume of interest that can be imaged, as well as the capability of performing 3D versus 2D imaging. The aforementioned technologies can produce representations of a 3D volume composed of approximately 1000 × 1000 × 1000 pixels, or 10^9 voxels. However, the lineal dimensions from vascular porosity to canaliculi span 100 μm to 1 nm, or volumetrically $10^5 \times 10^5 \times 10^5$, implying the need for at least 10^{15} voxels to concurrently image vascular, lacunar and canalicular features. Such digital processing is difficult with current desktop computational systems.

Electron microscopy has higher imaging resolution capabilities compared to imaging approaches based on photons or X-ray light. Scanning and transmission electron microscopy (SEM, TEM) can produce images with about 1-nm resolution (Table 1); however, both are limited in that they produce 2D images. The development of transmission electron microscopy computed tomography (TEM CT) and ultra-high voltage electron microscopy (UHVEM) has overcome this limitation, based on a methodology similar to X-ray CT. Three-dimensional renderings of osteocytes and their cell processes have been reported

NIH-PA Author Manuscript

NIH-PA Author Manuscript

NIH-PA Author Manuscript

using UHVEM at 8-nm resolution (Kamioka et al. 2009) and ~1–3 nm resolution (Kamioka et al. 2012). This approach allows for tomographic imaging of canaliculi beyond the capabilities of any other current technology. However, few UHVEM systems are available worldwide, and the volume of interest that can be imaged by this technique is limited due to the small penetration of electrons in calcified tissue, requiring energies on the order of MeV to penetrate 1–3 μm thick sections.

The recent developments of atomic force microscopy (AFM) and serial focused ion beam/scanning electron microscopy (FIB/SEM) seem to be well positioned to image both lacunae and canaliculi. AFM can produce 2D images of the lacunar-canalicular network at ~20 – 50 nm resolution (Table 1); however, different results are obtained when bone is embedded in polymethyl methacrylate or decalcified. FIB/SEM requires removing thin layers of the tissue (~10 nm) sequentially, producing a series of SEM images that are then used to produce a 3D rendering of the tissue. Despite being a destructive approach, FIB/SEM could provide essential 3D data on the lacunar-canalicular system and shed light on its role in osteocyte mechanotransduction. Figure 1 shows typical examples of three-dimensional imaging of vascular porosity using μCT (Cooper et al. 2003) and SR-μCT (Hannah et al. 2010), as well as osteocyte lacunae and canaliculi using confocal laser scanning microscopy (Sharma et al. 2012), serial FIB/SEM (Schneider et al. 2010; Stokes et al. 2005) and SEM (Kubek et al. 2010). Figure 2 displays two-dimensional, high-resolution imaging of vascular, lacunar and canalicular pores using AFM at different magnifications (Lin and Xu, 2011), and 2D high-resolution imaging of canaliculi using TEM (You et al., 2004). Imaging approaches requiring histological processing may contain artifacts produced during sectioning and dehydration of the tissue sample. A more detailed review of the technologies used for imaging of the lacunar-canalicular system can be found in Schneider et al. (2010).

VASCULAR AND LACUNAR-CANALICULAR POROSITIES

The vascular porosity has been documented to exhibit a wide range of values in human tissue, from 4% to more than 16%, while a much smaller range, 1 – 5%, has been reported in mice (Table 2). Using digitized images acquired with a video camera, Feik et al. (1997) reported an average vascular porosity close to 7% that was higher at older ages in both male and female human femurs. Using a similar methodology, Stein et al. (1999) also found the vascular porosity to be age-dependent, with an average of ~6% in the human femoral diaphysis of subjects aged 21 – 92 years. The average vascular porosity of human femurs measured using microradiography was found to be 8 – 10% in males and females (Bousson et al. 2000, 2001). Using μCT and microradiography, Cooper et al. (2004, 2007) also found an average vascular porosity of ~6 – 7% in the human femur, with variation as a function of age. Thomas et al. (2005) reported a large regional and age-dependent vascular porosity variability in the human femur, ranging from 4.5% (younger) to 16% (older). Using SR-μCT, Bousson et al. (2004) also found a relatively high vascular porosity (16%) in older females (mean age 87) in the femoral neck. While the femur has been analyzed more than any other bone, Renders et al. (2007) reported a vascular porosity of ~4% in the human mandibular condyle. In addition, Kingsmill et al. (2007) measured the vascular porosity using backscattered SEM at several skeletal sites, finding the most porous cortex to be the femoral neck, which had a mean vascular porosity (also referred to as cortical porosity) of 16%. In the mandible, the porosity varied depending in the site studied (3 – 11%), the vascular porosity of the fourth lumbar vertebrae was ~5%, and the vascular porosity in the iliac crest was ~8% (Kingsmill et al. 2007). In mice, μCT and SR-μCT were used in studies by Martin-Badosa et al. (2003) and Schneider et al. (2007, 2009) in which the vascular porosity in the femur was found to be in the range of ~1 – 5%. Clearly, the vascular porosity strongly depends on bone location, age, species, and resolution of the system employed to

NIH-PA Author Manuscript

NIH-PA Author Manuscript

NIH-PA Author Manuscript

measure it; fortunately, current high-resolution tomography imaging systems permit assessing the vascular porosity with accuracy and in three dimensions.

There are not many 3D measurements for the lacunar-canalicular porosity (LCP), which is more difficult to quantify compared to the vascular porosity because of its smaller size (Table 2). Using SR-μCT, Schneider et al. (2007) found the lacunar porosity in the femoral mid-diaphysis of B6 and C3/B6 mice to be ~1%, and Tommasini et al. (2012) reported the lacunar porosity to be 1.5% in the rat femoral diaphysis. Schneider et al. (2011) used serial FIB/SEM to measure the canalicular porosity (excluding the lacunar porosity) in the femoral mid-diaphysis of B6 mice, finding it to be < 1%. In contrast, and pointing out that canalicular volumes measured using confocal microscopy should only be used to assess relative differences between groups because of partial volume effects, Sharma et al. (2012) found a canalicular porosity of ~14% in the rat proximal tibia.

Water in the collagen-apatite porosity is bound to the mineral phase of bone (Neuman et al. 1953, Wehrli and Fernandez-Seara 2005) and is considered to have no significant effect on osteocyte mechanotransduction; thus, it is often not taken into account in interstitial fluid flow studies (Cowin 1999). Several tracer molecules of various sizes have been used to explore tracer movement through the bone interstitial fluid spaces, and to determine the pore size in the lacunar-canalicular system and the collagen-apatite porosity (Table 2). The most commonly used tracers have been ferritin, approximately 12 nm in diameter (Dillaman 1984, Montgomery et al. 1988, Qin et al. 1999, Wang et al. 2004, Ciani et al. 2005), horseradish peroxidase, approximately 6 nm in diameter, (Doty and Schofield 1972), microperoxidase, approximately 2 nm in diameter (Tanaka and Sakano 1985, Ayasaka et al. 1992, Knothe Tate et al. 1998b), and procion red and reactive red, < 1 nm in diameter (Knothe Tate et al. 1998a, Wang et al. 2004). The most recent literature (Wang et al. 2004, Ciani et al. 2005) has demonstrated that the effective pore size of the osteocyte glycocalyx lies between 6 and 12 nm because the tracer ferritin is excluded from the LCP (Table 2). The effective collagen-apatite pore size is believed to be less than 1 nm because tracers < 1 nm cannot penetrate the collagen-apatite porosity in mature bone (Table 2). Additional studies have shown that solute diffusion in the LCP and enhanced solute transport due to mechanical loading is dependent on the molecular weight and shape of the tracer (Tami et al. 2003, Li et al. 2009).

Lacunar-canalicular architecture

A number of microarchitectural parameters of the lacunar-canalicular system are now available in the literature due to the recent imaging advances described above (Table 3). The lacunar-canalicular microarchitecture includes the volumetric lacunar density, which represents the number of osteocyte lacuna measured per unit volume (#/mm^3), lacunar volume, lacunar length and depth, inter-lacuna separation, canaliculi diameter, areal canaliculi density or number of canaliculi per unit surface, and number of primary and secondary (branching) canaliculi emanating from a lacuna. The average number of osteocyte lacunae measured per unit volume has been reported to vary from $26 – 90\times10^3$ lacunae/mm^3 when considering the studies by Hannah et al. (2010), Tommasini et al. (2012), and Carter et al. (2012) from SR-μCT measurements, and by Sharma et al. (2012) using CLSM. Studies using CLSM and SR-μCT have found the average lacunar volume to fall in the range of 290 to 455 μm^3 (McCreadie et al. 2004, Hannah et al. 2010, Sharma et al. 2012, Carter et al. 2012). The lacuna length and width have been reported in the studies by Sugawara et al. (2005) and Vatsa (2008) using CLSM, in the work by Hannah et al. (2010) using SR-μCT, and in Lin and Xu (2011) using AFM. The average lacuna length varies between 9 and 29 μm, and the lacuna width varies from 2 to 8 μm. The inter-lacunar separation has been reported to vary between 22 and 40 μm in different species in CLSM studies by Sugawara et

NIH-PA Author Manuscript

NIH-PA Author Manuscript

NIH-PA Author Manuscript

al. (2005, 2011) and Sharma et al. (2012), and using SR-μCT in the study by Hannah et al. (2010). Canaliculi morphology measurements were reported in the early work of Marotti et al. (1985, 1990, 1995) and in several other more recent studies. The average canaliculi diameter spans a range of 100 to 700 nm, as reported in the works by Marotti (1990), You et al. (2004), Schneider et al. (2011) and Sharma et al. (2012) using electron microscopy, in the CLSM studies by Sugawara et al. (2005) and Sharma et al. (2012), and in the study by Lin and Xu (2011) using AFM. Canalicular diameter measurements are considered to be overestimated in studies using CLSM systems because of partial volume effects. The areal canaliculi density was reported in the SEM study by Marotti et al. (1995) and in the AFM work of Lin and Xu (2011) to vary between 0.5 and 0.9 canaliculi/μm^2. Finally, an average of 41 to 115 primary canaliculi per lacuna was reported in the studies by Sugawara et al. (2005), Beno et al. (2006), and Sharma et al. (2012) using CLSM and estimations from light microscopy measurements, as well as in the work by Schneider et al. (2011) using FIB/SEM. Secondary canaliculi, which may branch from the primary canaliculi directly connected to a lacuna, were found to be ~390 canaliculi per lacuna in Sharma et al. (2012), which is four times higher than the number of primary canaliculi reported in the same study (Table 3).

Vascular, lacunar-canalicular and collagen-apatite permeability of bone

The vascular permeability has been theoretically estimated using measurements of the vascular pore architecture, and experimentally measured using a traditional technique based on Darcy's law. This technique consists of measuring the volume of fluid flow per unit area and per unit time across a porous layer, which is then divided by the pore pressure gradient across the layer. Reported theoretical estimates and experimental measurements of permeability associated with the vascular porosity span several orders of magnitude (Table 4). Zhang et al. (1998a) analytically estimated the vascular permeability to be ~6×10^{-13} m^2. Johnson (1984) estimated the permeability *in vitro* after clearing the organic materials in the vascular channels of bovine bone to be in the range of $1 – 5 \times 10^{-14}$ m^2, and proposed a lower limit of the vascular permeability of bovine bone *in vivo* to be ~10–16 m^2. Rouhana et al. (1981), Malachanne et al. (2008), and Li et al. (1987) used the classical Darcy's method to measure the vascular permeability in bone. The permeability estimated by this method was found to be in the range of 10^{-11} to 10^{-17} m^2. The Malachanne et al. (2008) estimates were based on a combined experimental and finite element analysis approach that resulted in a vascular porosity permeability value on the order of 10^{-13} m^2.

Because Darcy permeability measurements are experimentally unfeasible for assessing the LCP permeability, the LCP permeability has been derived from theoretical approaches or from experimental measurements coupled with numerical/analytical approaches. One of the first analytical models was developed by Weinbaum et al. (1994) to study the small-scale fluid mechanics within the LCP using Brinkman's equation (Darcy's law and Stokes equation). This work also studied the fluid shear stress at the membrane cell surface and established a relationship between large-scale deformation of bone tissue due to external loading and fluid mechanics in the LCP using poroelasticity theory. For the treatment of the small-scale fluid mechanics within the LCP, a microscopic scale poroelasticity approach was used to estimate the permeability of a fiber-filled medium representing the pericellular space within a canaliculus, followed by a macroscopic-scale approach in the lacunar-canalicular system, to quantify the lacunar-canalicular permeability. The permeability of the fiber-filled medium in a single canaliculus, k_p, was determined following Tsay and Weinbaum (1991) as:

$$k_p = 0.0572 a_0^2 (\Delta / a_0)^{2.377}, \quad (1)$$

NIH-PA Author Manuscript

NIH-PA Author Manuscript

NIH-PA Author Manuscript

where a_0 is the radius of the pericellular fibers (~0.6 nm), and Δ is the effective spacing of the fibers of the pericellular matrix (~7 nm). Thus, the lacunar-canalicular permeability, k_{LC}, was estimated from the anatomical features of the LCP, assuming a regular array of osteocytes and homogenous canalicular distribution (Weinbaum et al. 1994):

$$k_{LC}=\frac{2\pi n a^4 q^3}{\gamma^3 L^2}\left\{A_1\left[I_1(\gamma/q)-qI_1(\gamma)\right]+B_1\left[qK_1(\gamma)-K_1(\gamma/q)\right]+\frac{\gamma\left(q^2-1\right)}{2q}\right\}, \quad (2)$$

where q is a dimensionless ratio between b and a, the radius of the canaliculus and the osteocyte process, respectively ($q = b/a$), L is the average spacing between two lacunae, n is the total number of canaliculi emanating from one lacuna, γ is a dimensionless length ratio between the canalicular radius and the square root of the permeability (associated boundary layer thickness) of a single canaliculus, $\gamma=b/\sqrt{k_P}$, and the parameters A_1 and B_1 were defined as

$$A_1=\frac{K_0(\gamma)-K_0(\gamma/q)}{I_0(\gamma/q)K_0(\gamma)-I_0(\gamma)K_0(\gamma/q)}, B_1=\frac{I_0(\gamma/q)-I_0(\gamma)}{I_0(\gamma/q)K_0(\gamma)-I_0(\gamma)K_0(\gamma/q)}, \quad (3)$$

where I_0, K_0, I_1 and K_1 are modified Bessel functions of the first and second kind.

Based on Weinbaum's ultrastructural model of the lacunar-canalicular system and Biot's poroelasticity theory, Zeng et al. (1994) provided an early estimate of the LCP permeability on the order of 10^{-20} to 10^{-22} m^2, Zhang et al. (1998a) reported a value of ~10^{-20} m^2, and Wang et al. (1999) found the LCP permeability of bovine bone to be ~10^{-20} m^2.

In addition to the approach proposed by Weinbaum et al. (1994), the lacunar-canalicular permeability has been estimated using the Carman-Kozeny geometric relationship between permeability and porosity. In the study by Goulet et al. (2009), the porosity and permeability values were determined using capillary and spherical-shell (Carman-Kozeny) models for the canalicular and lacunar microstructures, respectively. The Carman-Kozeny geometric permeability model for flow through concentric spheres is

$$k=\frac{\phi^3}{100K_0T_1(1-\phi)^2S_0^2}, \quad (4)$$

where K_0 is a shape factor generally considered to have a value between 2 and 3, T_1 is the tortuosity of the pore space (ratio of the actual length of the flow path to the straight length), S_0 is the surface area of the spherical shell:

$$S_0=\frac{4\pi\left(R_0^2-R_i^2\right)}{V_T}, \quad (5)$$

and the lacunar porosity φ is given by:

$$\phi=\frac{(4/3)\pi\left(R_0^3-R_i^3\right)}{V_T}, \quad (6)$$

where R_i is the radius of the osteocyte, R_o is the radius of the lacuna, and V_T is the total lacuna volume. Lemaire et al. (2012) also estimated the LCP permeability based on finite element analysis (FEA) and the Carman-Kozeny relation:

NIH-PA Author Manuscript

NIH-PA Author Manuscript

NIH-PA Author Manuscript

$$k \equiv \frac{\phi^3}{c(1-\phi)^2 A^2}, \quad (7)$$

where c is the Kozeny parameter, generally considered to be a linear function of the square of the canaliculi tortuosity, and A is the area of the solid-fluid interface in an elementary representative volume. Lemaire et al. (2012) reported the permeability to vary between 10^{-18} and 10^{-19} m^2 and also proposed a dimensional analysis using the squared value of the smallest possible pore size in the lacunar-canalicular system, estimating the minimum LCP permeability to be ~10^{-22} m^2. The FEA approach by Gururaja et al. (2005) obtained estimates of the LCP permeability in the radial and circumferential directions to be 10^{-22} and 10^{-21} m^2, respectively.

Among the experimental measurements coupled with numerical/analytical approaches, Smit et al. (2002) obtained an estimate of the LCP permeability on the order of 10^{-22} m^2 based on the best fit between finite element predictions and data from streaming potential measurements reported by Otter et al. (1992). Beno et al. (2006) estimated the LCP permeability of canine bone to vary from 10^{-19} m^2 to 10^{-22} m^2, and a study by Zhou et al. (2008) in mice found the LCP permeability to be on the order of 10^{-21} m^2. The LCP permeability of human bone was estimated by Oyen (2008) to be ~10^{-24} m^2 in water and 10^{-26} m^2 in polar solvents (methanol, ethanol, and acetone) using nanoindentation measurements and poroelasticity theory. Using the same nanoindentation technique and assuming the mineralized tissue material as compressible, Galli and Oyen (2009) estimated the LCP permeability of human bone to be 6.5×10^{-23} m^2. Canine LCP was measured in situ by Gardinier et al. (2010) and reported as 10^{-23} m^2.

A limitation associated with most studies based on perfusion of whole bone samples is that the resulting measurements correspond to the combination of the vascular porosity and LCP permeabilities because of the intermingling of the vascular and lacunar-canalicular pores. However, it is generally accepted that the estimated permeability in samples of millimeter size or larger is dominated by the vascular pores, which are bigger than the lacunar-canalicular pores. In order to eliminate the influence of the vascular permeability in experimental measurements of the lacunar-canalicular permeability, Gailani and Cowin (2008) proposed to perform the permeability measurement in samples containing the LCP only, such as a single osteon. An analytical solution of a saturated compressible poroelastic annular cylinder under an unconfined stress-relaxation test was developed, and predictions made by this model were compared to experimental stress-relaxation measurements made on isolated osteons *in vitro*, *i.e.* considering zero blood pressure (Gailani and Cowin, 2008). Curve fitting between data and experiments was used to obtain the LCP permeability without the influence of the vascular porosity in bovine bone, resulting in LCP permeability on the order of 10^{-24} to 10^{-25} m^2 (Gailani et al. 2009). Recently, the theoretical/experimental approach was extended to the case of harmonic loading of osteons to investigate the frequency dependence of the LCP permeability (Benalla et al. 2012).

Similar to the large variability in vascular permeability, the estimates of lacunar-canalicular permeability summarized above also exhibit a broad range of values, from 10^{-17} to 10^{-25} m^2, with a noticeable 2 – 3 orders of magnitude difference between the average permeability value obtained from theoretical approaches (10^{-17} to 10^{-20} m^2) and experimental/theoretical approaches (10^{-22} to 10^{-25} m^2) (Table 4). This large variability in the lacunar-canalicular permeability is likely influenced by theoretical assumptions and experimental errors associated with the measurement of a very small quantity. Major difficulties associated with the measurement of the lacunar-canalicular permeability are (a) the influence of the vascular

NIH-PA Author Manuscript

NIH-PA Author Manuscript

NIH-PA Author Manuscript

porosity in experimental measurements, (b) the challenge of performing direct measurements on samples with very small permeability and very small size (*i.e.*, samples 100 to 250 μm in diameter and 0.5 mm in height), (c) the time elapsed between sample isolation and permeability measurement, which results in lack of freshness of the tissue, (d) the imprecise knowledge of boundary conditions and the values for the key material parameters of the analytical model used to estimate the lacunar-canalicular permeability, and (e) not fully investigated hydroelectrochemical effects associated with fluid flow in canaliculi (Lemaire et al. 2012).

Vascular and lacunar-canalicular fluid pressure

As presented in previous sections, the porosities of bone are non-uniform and the sizes of the pores in the vascular and lacunar-canalicular domains differ by orders of magnitude. Therefore, the bone fluid pressures in the VP and LCP are expected to be significantly different. The pore size of the vascular porosity is sufficiently large to permit a rapid decay of a pressure pulse by diffusion, and thus should be a low-fluid-pressure domain. The fluid pressure magnitude in the vascular porosity domain is considered similar to the blood pressure in bone capillaries (40 to 60 mmHg, or correspondingly 5.3 kPa to 8 kPa) because an interstitial fluid pressure in the vascular porosity significantly greater than 40 to 60 mmHg would collapse these blood vessels, and a prolonged increase in the interstitial fluid pressure significantly above the blood pressure would deprive the tissue of oxygen and nutrients (Cowin 1999). On the other hand, the lacunar-canalicular system is a high-fluid-pressure domain because the pore size of the LCP is very small, leading to a slow decay of a pressure pulse. The drainage/imbibing of interstitial fluid in the LCP and vascular porosity has been estimated in the works by Zhang et al. (1998a, 1998b), Wang et al. (2000), Qin et al. (2002), Gururaja et al. (2005), and measured in Wang et al. (2005). Overall, these studies showed that the relaxation time of the lacunar-canalicular porosity occurs on a time scale ($\sim 10^{-3}$ s) that is much larger than the short pressure adjustment relaxation time for the vascular porosity ($\sim 10^{-6}$ s).

The bone fluid pressures in the vascular and lacunar-canalicular domains behave almost independently of each other. This notion seems counterintuitive because the vascular porosity and the lacunar-canalicular porosity are interconnected, occupying the same three-dimensional volume of bone tissue. However, Wang et al. (2003) reported that during venous stasis the mean intramedullary pressure is increased, but the amplitude of its pulsatile component is decreased, and therefore, the induced peak shear stress in the lacunar-canalicular system is reduced when compared to the normal condition. Goulet et al. (2009) used finite element analysis in an idealized cortical bone sample loaded at a frequency of 1 Hz to investigate the pore fluid pressure in the lacunar-canalicular system, and reported that the pressure generated with a canalicular permeability of 10^{-18} m^2 is unrealistic, since this fluid pressure would be insufficient to drive fluid against the trans-cortical pressure difference (~6 kPa). Moreover, Goulet et al. (2009) determined that pressure magnitude gradients produced in bone with permeabilities on the order of 10^{-20} m^2 are required to produce the fluid pressure necessary to convect fluid flow in the lacunar-canalicular system and allow fluid to flow against the trans-cortical pressure gradient. These results were consistent with measurements provided in the studies by Garner et al. (2000) and Buechner et al. (2001). Cowin et al. (2009) have shown analytically that the influence of the vascular porosity and lacunar-canalicular porosity on each other in terms of pressure change is less than 3%, and the vascular porosity pore pressure (considering a permeability on the order of 10^{-10} m^2) will slightly increase the total pressure in the LCP, which will cause a decrease in the fluid flow from the LCP by less than 6%. Recently, Li et al. (2010) experimentally demonstrated that despite the extreme importance of vasculature in bone physiology, vascular pressure itself does not enhance acute solute transport within the lacunar-

NIH-PA Author Manuscript

NIH-PA Author Manuscript

NIH-PA Author Manuscript

canalicular system. Overall, these fluid pressure considerations suggest that the VP and LCP function almost independently, with the prime mechanical influences for the two porosities being very different, as are the time scales of their response.

Analytical and computational bone fluid flow models

In addition to providing estimates of pore fluid pressures and permeabilities that could otherwise not be measured, analytical and finite element models of the lacunar-canalicular system have been of great utility to better understand many other aspects of bone interstitial fluid flow. The early work of Zeng et al. (1994) predicted the fluid shear stress and the streaming potentials at the surface of osteocyte processes in the LCP when an osteon is subjected to mechanical loading. The study by Cowin et al. (1995) determined that experimentally observed strain-generated potentials (SGPs) are created in the LCP and not within the collagen-apatite porosity. Wang et al. (1999) developed a two-porosity (LCP and VP) poroelastic model to explain the local variations measured in strain-generated potentials during quasi static or dynamic loading of bone reported by Starkebaum et al. (1979) and demonstrated that the bone fluid relaxes primarily through the vascular porosity. The study by Wang et al. (1999) took into account the fact that the VP is several orders of magnitude larger in characteristic pore size than the LCP and has a much lower pressure, and demonstrated that the consideration of the two porosities is necessary to obtain correct local bone fluid flow patterns as a function of the frequency of the applied bending loading in bone. The analytical solution for the pressure term obtained in the model by Wang et al. (1999) was used to investigate tracer concentrations in the lacunar-canalicular porosity, demonstrating that permeability and loading frequency are key parameters of fluid transport (Wang et al., 2000). The study by Smit et al. (2002) used Biot's poroelasticity and experimental data from the literature to estimate a full set of poroelastic constants for a linear isotropic description of cortical bone as a two-level porous medium. A series of papers (You et al. 2001, Han et al. 2004, Wang et al. 2007) refined the model presented in Weinbaum et al (1994) using the latest ultrastructural data for the osteocyte processes and the tethering elements connecting them to the canalicular wall. Importantly, these models proposed that during fluid flow the mechanotransduction and strain amplification in osteocytes may occur due to deformation of these tethering elements, rather than the previously proposed fluid-shear hypothesis. In the study by Goulet et al. (2008), the influence of the VP on fluid flow, pore fluid pressure and solute transport was investigated using FEA in an anatomically accurate tibial section created from μCT images. Numerical simulations indicated the genesis of large local pressure gradients surrounding the vascular canals, in agreement with the studies by Wang et al. (1999). Mechanical loading had a significant effect on fluid flow velocities and tracer perfusion, mainly in the bone region with the highest compressive magnitude, in which the fluid exchange between the vascular canals and the lacunar-canalicular porosity are maximal.

Recent theoretical/experimental studies by Wang et al. (2005) and Zhou et al. (2008) using fluorescence recovery after photobleaching (FRAP) have significantly advanced the field by visualizing and quantifying fluid and solute flows in situ and *in vivo*. In this work, a model was developed to investigate both fluid and solute flows in the lacunar-canalicular system while a cyclic intermittent mechanical loading was applied to the entire bone. Both bone morphology and microstructural parameters of the lacunar-canalicular system were incorporated in the model, and the effects of the pericellular matrix on both fluid and solute flows were considered. Lemaire et al. (2008) studied the influence of a fibrous pericellular matrix on the cortical interstitial fluid movement with hydroelectrochemical effects, demonstrating that the presence of the fibrous matrix tends to reduce the fluid flow considerably and that the role of osmotic and electro-osmotic effects needs to be taken into account.

NIH-PA Author Manuscript

NIH-PA Author Manuscript

NIH-PA Author Manuscript

While several poroelastic studies have been developed to investigate fluid flow in porous media with two different characteristic pore sizes (lacunar and canalicular porosities, or vascular and lacunarcanalicular porosities), most studies have not considered the effect of having these porosities interconnected. Cowin et al. (2009) introduced the nested porosity concept for bone under harmonic loading and Gailani and Cowin (2011) for bone excited using a ramp loading, in which the hierarchical structure of cortical bone was modeled using two porosity levels, the VP and the LCP. The model could be described as a set of nested porosities like a set of Russian dolls of decreasing sizes placed one inside another. The proposed nested structure is a generalization of traditional poroelasticity to a hierarchical system of uniform porosity levels that allows fluid exchange between the different levels.

Load-induced fluid flow and the permeability of the lacunar-canalicular system has also been investigated in combined poroelasticity/FEA approaches using representative geometries of the lacunar-canalicular system, and more recently in models generated from high-resolution tomographic images of the lacunar-canalicular system (~1 nm pixel size). The poroelasticity/FEA study by Mak et al. (1997) was developed to study the contributions from various hierarchical flow channels in bone, including flow through the collagen-apatite, lacunar-canalicular and vascular porosities. The model included three interconnected osteons with only a few canaliculi under bending loading and the fluid was free to flow into the collagen-apatite porosity. The effect of the lacunar-canalicular porosity in this model is believed to be underestimated due to the limited number of channels considered in the simulation. Steck et al. (2003) developed a FEA model employing a two-step approach to study the influence of load-induced fluid flow on molecular transport in bone. Given these theoretical data in conjunction with experimental data from tibiae under four point-bending loads *in vivo*, it was found that mechanical loading modulates local flow distribution and concentration gradients within the tissue.

The study by Gururaja et al. (2005) presented a two-dimensional FEA model of a periodic array of lacunae and their surrounding systems of canaliculi to quantify local fluid flow characteristics in the vicinity of a single lacuna. The results in this study showed that there is a gradient of fluid pressures in the canaliculi that leads to flow into and out of the lacuna due to the heterogeneity of the deformation around a lacuna. Fornells et al. (2007) developed a dual-porosity finite element model of the VP and the LCP. This mixture theory-based model is a macroscopic approach and the Haversian canals are not physically considered, but the fluid flow fields predicted were similar to those obtained with previous microscopic models. The results at both scales were in agreement with previous models that either considered the macroscopic or the microscopic scale separately.

Remond et al. (2008) built a one-level porosity FEA model based on cylindrical geometry of the osteon using transverse isotropic mechanical properties, linear elasticity, and Darcy's law, with both fluid and solid phases considered as compressible. It was found that a permeability gradient affects the fluid pressure more than the velocity profile, the fluid flow response depends on the loading strain rate, and a Poisson's ratio gradient affects both fluid pressure and fluid velocity. Nguyen et al. (2009) presented a numerical approach to study interstitial fluid flow in cortical bone modeled as a saturated anisotropic poroelastic material containing three-dimensional periodic groups of osteons. Unlike many previous models, the cement line was not considered to be impermeable, and the fluid shear stress variations were studied for various harmonic loading conditions and geometrical or physical bone matrix parameters, and analyzed in the frequency domain. In the poroelasticity/FEA study by Goulet et al. (2009), the pore fluid pressure and fluid shear stress were calculated in response to simulated mechanical loading applied over a range of frequencies. Pore fluid pressures and fluid shear stress magnitudes were in agreement with previous experimental

NIH-PA Author Manuscript

NIH-PA Author Manuscript

NIH-PA Author Manuscript

and theoretical studies, confirming the importance of high-magnitude low-frequency loading on bone interstitial fluid flow.

Anderson and Knothe Tate (2008) used computational fluid dynamics to estimate fluid velocities, pressures, and wall shear stresses on the osteocyte process surface in two- and three-dimensional models generated from TEM images and idealized pericellular canalicular geometries. The study showed that the naturally occurring protrusions of the pericellular space produced localized stress spikes on the surface of the osteocyte process, up to five times those predicted using idealized geometries, which are close to the stress level required to trigger cell responses *in vitro*. In another recent study, Kamioka et al. (2012) analyzed the microscale fluid flow within a human osteocyte canaliculus the Lattice Boltzman method (3.4 and 7.0 nm lattice length) and a realistic 3D model generated from high-resolution UHVEM images (~1–3 nm resolution). At this resolution, the canalicular wall shows a highly irregular surface accompanied by protruding axisymetric structures (apparently collagen fibers), which influence the fluid flow profile within the canaliculi, leading to highly inhomogenous flow patterns of the Newtonian interstitial fluid in the canaliculus (Kamioka et al. 2012).

Summary remarks

This review has summarized the imaging technologies used to visualize bone porosities and architecture at several scale lengths, recent studies aimed to measure the vascular porosity and the lacunar-canalicular microarchitecture as well as the fluid pressure and permeability in the vascular and lacunar-canalicular domains, and the recent development of models to represent the interchange of fluids between these two porosities. Some key points of this review are highlighted as follows:

1. Recent developments in imaging technologies are opening new avenues toward a more precise characterization of the vascular and lacunar-canalicular porosities in bone. These technologies are characterized by higher resolution and the capability of three-dimensional imaging, such as CLSM, AFM, FIB/SEM, TEM CT, UHVEM, μCT, nanoCT, TXM CT and SR-μCT.
2. 3D characterization of the lacunar-canalicular micro/nano architecture is now possible at resolutions in the ~ 1 – 10 nm range, providing exquisite details of the lacunar-canalicular environment for improved fluid flow modeling.
3. Data on vascular porosity are fairly consistent in mice and more variable in human tissue, possibly because of the different age of human subjects from which the samples were obtained. The lacunar-canalicular porosity measurements reported to date vary with the imaging technique utilized.
4. Analytical studies of the vascular porosity have shown that the permeability in this domain cannot be smaller than 10^{-14} m^2, otherwise the interstitial fluid pressure would be higher than the pressure in the blood vessels, which would collapse and become impaired. Analytical/numerical studies have also shown that the permeability in the lacunar-canalicular domain should be ~10^{-20} m^2 or smaller to be able to produce fluid flow inside canaliculi, and stimulate osteocytes.
5. Measuring the fluid flow in situ is possible using FRAP. Tracer studies have shown that the pore size in the collagen-apatite domain is likely less than 1 nm.
6. There is a 2 – 3 order of magnitude difference between theoretical and experimental/theoretical measurements of the lacunar-canalicular permeability. Such variation may be a consequence of theoretical assumptions/boundary conditions, as well as experimental errors associated with the nested porosities in

NIH-PA Author Manuscript

NIH-PA Author Manuscript

NIH-PA Author Manuscript

bone, which are difficult to isolate, the freshness of the tissue tested, and the presence of the soft tissues inside the lacunae and canaliculi, among other factors.

7. Recent analytical models have been developed to take into account the effect of the hierarchical porosities in bone, and thus the effect of the pore pressure and permeability of one level to the next level of porosity. However, more realistic models at the microstructural level are needed.

Acknowledgments

This research has been supported by NIH grants ARRA RCI HL101151, AG034198, and AR052866, NSF grants MRI 0723027 and MRI 1229449, and a grant from the Arthritis Foundation (AF229767).

References

Anderson EJ, Kreuzer SM, Small O, Knothe Tate ML. Pairing computational and scaled physical models to determine permeability as a measure of cellular communication in micro- and nano-scale pericellular spaces. Microfluidics and Nanofluidics. 2008; 4(3):193–204.

Anderson EJ, Knothe Tate ML. Idealization of pericellular fluid space geometry and dimension results in a profound underprediction of nano-microscale stresses imparted by fluid drag on osteocytes. Journal of Biomechanics. 2008; 41(8):1736–1746. [PubMed: 18482728]

Ayasaka N, Kondo T, Goto T, Kido MA, Nagata E, Tanaka T. Differences in the Transport-Systems between Cementocytes and Osteocytes in Rats Using Microperoxidase as a Tracer. Archives of Oral Biology. 1992; 37(5):363–369. [PubMed: 1610305]

Benalla M, Cardoso L, Cowin SC. Analytical basis for the determination of the lacunar-canalicular permeability of bone using cyclic loading. Biomech Model Mechanobiol. 2012; 11(6):767–780. [PubMed: 21959747]

Beno T, Yoon YJ, Cowin SC, Fritton SP. Estimation of bone permeability using accurate microstructural measurements. J Biomech. 2006; 39(13):2378–2387. [PubMed: 16176815]

Bousson V, Bergot C, Meunier A, Barbot F, Parlier-Cuau C, Laval-Jeantet AM, Laredo JD. CT of the middiaphyseal femur: cortical bone mineral density and relation to porosity. Radiology. 2000; 217(1):179–187. [PubMed: 11012442]

Bousson V, Meunier A, Bergot C, Vicaut E, Rocha MA, Morais MH, Laval-Jeantet AM, Laredo JD. Distribution of intracortical porosity in human midfemoral cortex by age and gender. J Bone Miner Res. 2001; 16(7):1308–1317. [PubMed: 11450707]

Bousson V, Peyrin F, Berot C, Hausard M, Sautet A, Laredo JD. Cortical bone in the human femoral neck: Three-dimensional appearance and porosity using synchrotron radiation. Journal of Bone and Mineral Research. 2004; 19(5):794–801. [PubMed: 15068503]

Buechner PM, Lakes RS, Swan C, Brand RA. A broadband viscoelastic spectroscopic study of bovine bone: implications for fluid flow. Ann Biomed Eng. 2001; 29(8):719–728. [PubMed: 11556728]

Burger EH, Kleinnulend J, Vanderplas A, Nijweide PJ. Function of Osteocytes in Bone - Their Role in Mechanotransduction. Journal of Nutrition. 1995; 125(7):S2020–S2023.

Carter Y, Thomas CD, Clement JG, Peele AG, Hannah K, Cooper DM. Variation in Osteocyte Lacunar Morphology and Density in the Human Femur - a Synchrotron Radiation Micro-CT study. Bone. 2012 pii: S8756-3282(12)01234-3. doi: 10.1016/j.bone.2012.09.010. [Epub ahead of print].

Ciani C, Doty SB, Fritton SP. Mapping bone interstitial fluid movement: displacement of ferritin tracer during histological processing. Bone. 2005; 37(3):379–387. [PubMed: 15964255]

Cooper DM, Matyas JR, Katzenberg MA, Hallgrimsson B. Comparison of microcomputed tomographic and microradiographic measurements of cortical bone porosity. Calcif Tissue Int. 2004; 74(5):437–447. [PubMed: 14961208]

Cooper DM, Turinsky AL, Sensen CW, Hallgrimsson B. Quantitative 3D analysis of the canal network in cortical bone by micro-computed tomography. Anat Rec B New Anat. 2003; 274(1):169–179. [PubMed: 12964207]

NIH-PA Author Manuscript

NIH-PA Author Manuscript

NIH-PA Author Manuscript

Cooper DML, Thomas CDL, Clement JG, Turinsky AL, Sensen CW, Hallgrimsson B. Age-dependent change in the 3D structure of cortical porosity at the human femoral midshaft. Bone. 2007; 40(4): 957–965. [PubMed: 17223618]

Cowin SC. Bone poroelasticity. J Biomech. 1999; 32(3):217–238. [PubMed: 10093022]

Cowin SC, Gailani G, Benalla M. Hierarchical poroelasticity: movement of interstitial fluid between porosity levels in bones. Philos Transact A Math Phys Eng Sci. 2009; 367(1902):3401–3444.

Cowin SC, Mosssalentijn L, Moss ML. Candidates for the Mechanosensory System in Bone. Journal of Biomechanical Engineering-Transactions of the Asme. 1991; 113(2):191–197.

Cowin SC, Weinbaum S, Zeng Y. A case for bone canaliculi as the anatomical site of strain generated potentials. J Biomech. 1995; 28(11):1281–1297. [PubMed: 8522542]

Dillaman RM. Movement of ferritin in the 2-day-old chick femur. Anat Rec. 1984; 209(4):445–453. [PubMed: 6476415]

Dillaman RM, Roer RD, Gay DM. Fluid movement in bone: theoretical and empirical. J Biomech. 1991; 24(Suppl 1):163–177. [PubMed: 1791176]

Doty, SB.; Schofield, BH. Metabolic and structural changes within osteocytes of rat bone. In: Talmage, RV.; Munson, PL., editors. Calcium, Parathyroid Hormone and the Calcitonins. Elsevier; Amsterdam: 1972. p. 353-364.

Feik SA, Thomas CD, Clement JG. Age-related changes in cortical porosity of the midshaft of the human femur. J Anat. 1997; 191(Pt 3):407–416. [PubMed: 9418997]

Fornells P, Garcia-Aznar JM, Doblare M. A finite element dual porosity approach to model deformation-induced fluid flow in cortical bone. Ann Biomed Eng. 2007; 35(10):1687–1698. [PubMed: 17616819]

Fritton SP, Weinbaum S. Fluid and Solute Transport in Bone: Flow-Induced Mechanotransduction. Annu Rev Fluid Mech. 2009; 41:347–374. [PubMed: 20072666]

Galli M, Oyen ML. Fast identification of poroelastic parameters from indentation test. Comput Model Eng Sci. 2009; 48:241–270.

Gailani G, Benalla M, Mahamud R, Cowin SC, Cardoso L. Experimental determination of the permeability in the lacunar-canalicular porosity of bone. J Biomech Eng. 2009; 131(10):101007. [PubMed: 19831477]

Gailani G, Cowin SC. The unconfined compression of a porous annular cylindrical disk. J. of Mech. of Mater. 2008; 40(6):507–523.

Gailani G, Cowin SC. Ramp loading in Russian doll poroelasticity. J. Mech. Phys. Solids. 2011; 53:103–120.

Gardinier JD, Townend CW, Jen KP, Wu Q, Duncan RL, Wang L. In situ permeability measurement of the mammalian lacunar-canalicular system. Bone. 2010; 46(4):1075–1081. [PubMed: 20080221]

Garini Y, Vermolen BJ, Young IT. From micro to nano: recent advances in high-resolution microscopy. Curr Opin Biotechnol. 2005; 16(1):3–12. [PubMed: 15722009]

Garner E, Lakes R, Lee T, Swan C, Brand R. Viscoelastic dissipation in compact bone: implications for stress-induced fluid flow in bone. J Biomech Eng. 2000; 122(2):166–172. [PubMed: 10834157]

Goulet GC, Hamilton N, Cooper DM, Coombe D, Tran D, Martinuzzi R, Zernicke RF. Influence of vascular porosity on fluid flow and nutrient transport in loaded cortical bon. J Biomech. 2008; 41(10):2169–75. [PubMed: 18533159]

Goulet GC, Coombe D, Martinuzzi RJ, Zernicke RF. Poroelastic evaluation of fluid movement through the lacunocanalicular system. Ann Biomed Eng. 2009; 37(7):1390–1402. [PubMed: 19415492]

Gururaja S, Kim HJ, Swan CC, Brand RA, Lakes RS. Modeling deformation-induced fluid flow in cortical bone's canalicular-lacunar system. Ann Biomed Eng. 2005; 33(1):7–25. [PubMed: 15709702]

Han Y, Cowin SC, Schaffler MB, Weinbaum S. Mechanotransduction and strain amplification in osteocyte cell processes. Proc Natl Acad Sci U S A. 2004; 101(47):16689–94. [PubMed: 15539460]

NIH-PA Author Manuscript

NIH-PA Author Manuscript

NIH-PA Author Manuscript

Hannah KM, Thomas CDL, Clement JG, De Carlo F, Peele AG. Bimodal distribution of osteocyte lacunar size in the human femoral cortex as revealed by micro-CT. Bone. 2010; 47(5):866–871. [PubMed: 20691298]

Heintzmann R, Ficz G. Breaking the resolution limit in light microscopy. Brief Funct Genomic Proteomic. 2006; 5(4):289–301. [PubMed: 17170013]

Hell SW. Far-field optical nanoscopy. Science. 2007; 316(5828):1153–1158. [PubMed: 17525330]

Johnson MW. Behavior of fluid in stressed bone and cellular stimulation. Calcif Tissue Int. 1984; 36(Suppl 1):S72–76. [PubMed: 6430527]

Kameo Y, Adachi T, Sato N, Hojo M. Estimation of bone permeability considering the morphology of lacunocanalicular porosity. J Mech Behav Biomed Mater. 2010; 3(3):240–248. [PubMed: 20142108]

Kamioka H, Murshid SA, Ishihara Y, Kajimura N, Hasegawa T, Ando R, Sugawara Y, Yamashiro T, Takaoka A, Takano-Yamamoto T. A method for observing silver-stained osteocytes in situ in 3-μm sections using ultra-high voltage electron microscopy tomography. Microsc Microanal. 2009; 15:373–383.

Kamioka H, Kameo Y, Imai Y, Bakker AD, Bacabac RG, Yamada N, Takaoka A, Yamashiro T, Adachi T, Klein-Nulend J. Microscale fluid flow analysis in a human osteocyte canaliculus using a realistic high-resolution image-based three-dimensional model. Integrative Biology. 2012 (published on the web). DOI: 10.1039/c2ib20092a.

Kingsmill VJ, Gray CM, Moles DR, Boyde A. Cortical vascular canals in human mandible and other bones. J Dent Res. 2007; 86(4):368–372. [PubMed: 17384034]

Knothe Tate ML, Knothe U, Niederer P. Experimental elucidation of mechanical load-induced fluid flow and its potential role in bone metabolism and functional adaptation. Am J Med Sci. 1998a; 316(3):189–195. [PubMed: 9749561]

Knothe Tate ML, Niederer P, Knothe U. In vivo tracer transport through the lacunocanalicular system of rat bone in an environment devoid of mechanical loading. Bone. 1998b; 22(2):107–117. [PubMed: 9477233]

Knothe Tate ML, Steck R, Forwood MR, Niederer P. In vivo demonstration of load-induced fluid flow in the rat tibia and its potential implications for processes associated with functional adaptation. J Exp Biol. 2000; 203(Pt 18):2737–2745. [PubMed: 10952874]

Kubek DJ, Gattone VH, Allen MR. Methodological Assessment of Acid-Etching for Visualizing the Osteocyte Lacunar-Canalicular Networks Using Scanning Electron Microscopy. Microscopy Research and Technique. 2010; 73(3):182–186. [PubMed: 19725069]

Lemaire T, Lemonnier S, Naili S. On the paradoxical determinations of the lacuno-canalicular permeability of bone. Biomech Model Mechanobiol. 2012; 11(7):933–46. [PubMed: 22198036]

Lemaire T, Naili S, Remond A. Study of the influence of fibrous pericellular matrix in the cortical interstitial fluid movement with hydroelectrochemical effects. J Biomech Eng. 2008; 130(1): 011001–011001-11. [PubMed: 18298177]

Li GP, Bronk JT, An KN, Kelly PJ. Permeability of cortical bone of canine tibiae. Microvasc Res. 1987; 34(3):302–310. [PubMed: 2448591]

Li W, Gardinier JD, Price C, Wang LY. Does blood pressure enhance solute transport in the bone lacunarcanalicular system? Bone. 2010; 47(2):353–359. [PubMed: 20471508]

Li W, You L, Schaffler MB, Wang L. The dependency of solute diffusion on molecular weight and shape in intact bone. Bone. 2009; 45(5):1017–1023. [PubMed: 19647808]

Lin Y, Xu S. AFM analysis of the lacunar-canalicular network in demineralized compact bone. Journal of Microscopy. 2011; 241(3):291–302. [PubMed: 21118225]

Mak AF, Huang DT, Zhang JD, Tong P. Deformation-induced hierarchical flows and drag forces in bone canaliculi and matrix microporosity. J Biomech. 1997; 30(1):11–18. [PubMed: 8970919]

Malachanne E, Dureisseix D, Canadas P, Jourdan F. Experimental and numerical identification of cortical bone permeability. J Biomech. 2008; 41(3):721–725. [PubMed: 18023447]

Marotti, G. The original contributions of the scanning electron microscope to the knowledge of bone structure. In: Bonucci, E.; Motta, PM., editors. Ultrastructure of Skeletal Tissues. Kluwer Academic; Boston: 1990. p. 19-39.

NIH-PA Author Manuscript

NIH-PA Author Manuscript

NIH-PA Author Manuscript

Marotti G, Ferretti M, Remaggi F, Palumbo C. Quantitative evaluation on osteocyte canalicular density in human secondary osteons. Bone. 1995; 16(1):125–128. [PubMed: 7742070]

Marotti G, Muglia MA, Zaffe D. A SEM study of osteocyte orientation in alternately structured osteons. Bone. 1985; 6(5):331–334. [PubMed: 4096864]

Martin-Badosa E, Amblard D, Nuzzo S, Elmoutaouakkil A, Vico L, Peyrin F. Excised bone structures in mice: Imaging at three-dimensional synchrotron radiation micro CT. Radiology. 2003; 229(3): 921–928. [PubMed: 14657323]

McCreadie BR, Hollister SJ, Schaffler MB, Goldstein SA. Osteocyte lacuna size and shape in women with and without osteoporotic fracture. J Biomech. 2004; 37(4):563–572. [PubMed: 14996569]

McNamara LM, Majeska RJ, Weinbaum S, Friedrich V, Schaffler MB. Attachment of osteocyte cell processes to the bone matrix. Anat Rec (Hoboken). 2009; 292(3):355–363. [PubMed: 19248169]

Montgomery RJ, Sutker BD, Bronk JT, Smith SR, Kelly PJ. Interstitial fluid flow in cortical bone. Microvasc Res. 1988; 35(3):295–307. [PubMed: 3393091]

Neuman WF, Toribara TY, Mulryan BJ. The Surface Chemistry of Bone .7. The Hydration Shell. Journal of the American Chemical Society. 1953; 75(17):4239–4242.

Nguyen VH, Lemaire T, Naili S. Numerical study of deformation-induced fluid flows in periodic osteonal matrix under harmonic axial loading. Comptes Rendus Mecanique. 2009; 337(5):268–276.

Otter MW, Palmieri VR, Wu DD, Seiz KG, MacGinitie LA, Cochran GV. A comparative analysis of streaming potentials in vivo and in vitro. J Orthop Res. 1992; 10(5):710–719. [PubMed: 1500983]

Oyen ML. Poroelastic nanoindentation responses of hydrated bone. Journal of Materials Research. 2008; 23(5):1307–1314.

Piekarski K, Munro M. Transport Mechanism Operating between Blood-Supply and Osteocytes in Long Bones. Nature. 1977; 269(5623):80–82. [PubMed: 895891]

Price C, Zhou XZ, Li W, Wang LY. Real-Time Measurement of Solute Transport Within the Lacunar-Canalicular System of Mechanically Loaded Bone: Direct Evidence for Load-Induced Fluid Flow. Journal of Bone and Mineral Research. 2011; 26(2):277–285. [PubMed: 20715178]

Qin L, Mak AT, Cheng CW, Hung LK, Chan KM. Histomorphological study on pattern of fluid movement in cortical bone in goats. Anat Rec. 1999; 255(4):380–387. [PubMed: 10409810]

Qin YX, Lin W, Rubin C. The pathway of bone fluid flow as defined by in vivo intramedullary pressure and streaming potential measurements. Ann Biomed Eng. 2002; 30(5):693–702. [PubMed: 12108843]

Remaggi F, Cane V, Palumbo C, Ferretti M. Histomorphometric study on the osteocyte lacuno-canalicular network in animals of different species. I. Woven-fibered and parallel-fibered bones. Ital J Anat Embryol. 1998; 103(4):145–155. [PubMed: 9882957]

Remond A, Naili S, Lemaire T. Interstitial fluid flow in the osteon with spatial gradients of mechanical properties: a finite element study. Biomechanics and Modeling in Mechanobiology. 2008; 7(6): 487–495. [PubMed: 17990014]

Renders GA, Mulder L, van Ruijven LJ, van Eijden TM. Porosity of human mandibular condylar bone. J Anat. 2007; 210(3):239–248. [PubMed: 17331174]

Rouhana SW, Johnson MW, Chakkalakal DA, Harper RA. Permeability of the osteocyte lacunocanalicular compact bone. Joint ASME-ASCE Conf. Biomech. Symp. AMD. 1981; 43:169–172.

Schneider P, Krucker T, Meyer E, Ulmann-Schuler A, Weber B, Stampanoni M, Muller R. Simultaneous 3D Visualization and Quantification of Murine Bone and Bone Vasculature Using Micro-Computed Tomography and Vascular Replica. Microscopy Research and Technique. 2009; 72(9):690–701. [PubMed: 19360841]

Schneider P, Meier M, Wepf R, Muller R. Towards quantitative 3D imaging of the osteocyte lacuno-canalicular network. Bone. 2010; 47(5):848–858. [PubMed: 20691297]

Schneider P, Meier M, Wepf R, Muller R. Serial FIB/SEM imaging for quantitative 3D assessment of the osteocyte lacuno-canalicular network. Bone. 2011; 49(2):304–311. [PubMed: 21514408]

Schneider P, Stauber M, Voide R, Stampanoni M, Donahue LR, Muller R. Ultrastructural properties in cortical bone vary greatly in two inbred strains of mice as assessed by synchrotron light based

NIH-PA Author Manuscript

NIH-PA Author Manuscript

NIH-PA Author Manuscript

micro- and Nano-CT. Journal of Bone and Mineral Research. 2007; 22(10):1557–1570. [PubMed: 17605631]

Sharma D, Ciani C, Marin PA, Levy JD, Doty SB, Fritton SP. Alterations in the osteocyte lacunarcanalicular microenvironment due to estrogen deficiency. Bone. 2012; 51(3):488–97. [PubMed: 22634177]

Smit TH, Huyghe JM, Cowin SC. Estimation of the poroelastic parameters of cortical bone. J Biomech. 2002; 35(6):829–835. [PubMed: 12021003]

Steck R, Niederer P, Knothe Tate ML. A finite element analysis for the prediction of load-induced fluid flow and mechanochemical transduction in bone. J Theor Biol. 2003; 220(2):249–259. [PubMed: 12468296]

Stein MS, Feik SA, Thomas CD, Clement JG, Wark JD. An automated analysis of intracortical porosity in human femoral bone across age. J Bone Miner Res. 1999; 14(4):624–632. [PubMed: 10234585]

Stokes DJ, Tong JR, Juhasz J, Midgley PA, Best SM. Characterisation and 3D Visualisation of Biomaterials and Tissues using Focused Ion Beam (E)SEM. Microsc Microanal. 2005; 11:1260–1261.

Sugawara Y, Kamioka H, Honjo T, Tezuka K, Takano-Yamamoto T. Three-dimensional reconstruction of chick calvarial osteocytes and their cell processes using confocal microscopy. Bone. 2005; 36(5):877–883. [PubMed: 15820146]

Sugawara Y, Ando R, Kamioka H, Ishihara Y, Honjo T, Kawanabe N, Kurosaka H, Takano-Yamamoto T, Yamashiro T. The three-dimensional morphometry and cell-cell communication of the osteocyte network in chick and mouse embryonic calvaria. Calcif Tissue Int. 2011; 88(5):416–424. [PubMed: 21340572]

Swan CC, Lakes RS, Brand RA, Stewart KJ. Micromechanically based poroelastic modeling of fluid flow in Haversian bone. J Biomech Eng. 2003; 125(1):25–37. [PubMed: 12661194]

Tami AE, Schaffler MB, Knothe Tate ML. Probing the tissue to subcellular level structure underlying bone's molecular sieving function. Biorheology. 2003; 40(6):577–590. [PubMed: 14610309]

Tanaka T, Sakano A. Differences in Permeability of Microperoxidase and Horseradish-Peroxidase into the Alveolar Bone of Developing Rats. Journal of Dental Research. 1985; 64(6):870–876. [PubMed: 3858312]

Thomas CD, Feik SA, Clement JG. Regional variation of intracortical porosity in the midshaft of the human femur: age and sex differences. J Anat. 2005; 206(2):115–125. [PubMed: 15730477]

Tommasini SM, Trinward A, Acerbo AS, De Carlo F, Miller LM, Judex S. Changes in intracortical microporosities induced by pharmaceutical treatment of osteoporosis as detected by high resolution micro-CT. Bone. 2012; 50(3):596–604. [PubMed: 22226688]

Vatsa A, Breuls RG, Semeins CM, Salmon PL, Smit TH, Klein-Nulend J. Osteocyte morphology in fibula and calvaria --- is there a role for mechanosensing? Bone. 2008; 43(3):452–458. [PubMed: 18625577]

Wang L, Ciani C, Doty SB, Fritton SP. Delineating bone's interstitial fluid pathway in vivo. Bone. 2004; 34(3):499–509. [PubMed: 15003797]

Wang L, Cowin SC, Weinbaum S, Fritton SP. Modeling tracer transport in an osteon under cyclic loading. Ann Biomed Eng. 2000; 28(10):1200–1209. [PubMed: 11144981]

Wang L, Fritton SP, Cowin SC, Weinbaum S. Fluid pressure relaxation depends upon osteonal microstructure: modeling an oscillatory bending experiment. J Biomech. 1999; 32(7):663–672. [PubMed: 10400353]

Wang LY, Fritton SP, Weinbaum S, Cowin SC. On bone adaptation due to venous stasis. Journal of Biomechanics. 2003; 36(10):1439–1451. [PubMed: 14499293]

Wang LY, Wang YL, Han YF, Henderson SC, Majeska RJ, Weinbaum S, Schaffler MB. In situ measurement of solute transport in the bone lacunar-canalicular system. Proceedings of the National Academy of Sciences of the United States of America. 2005; 102(33):11911–11916. [PubMed: 16087872]

Wang Y, McNamara LM, Schaffler MB, Weinbaum S. A model for the role of integrins in flow induced mechanotransduction in osteocytes. Proc Natl Acad Sci U S A. 2007; 104(40):15941–15946. [PubMed: 17895377]

NIH-PA Author Manuscript

NIH-PA Author Manuscript

NIH-PA Author Manuscript

Wehrli FW, Fernandez-Seara MA. Nuclear magnetic resonance studies of bone water. Ann Biomed Eng. 2005; 33(1):79–86. [PubMed: 15709708]

Weinbaum S, Cowin SC, Zeng Y. A model for the excitation of osteocytes by mechanical loading-induced bone fluid shear stresses. J Biomech. 1994; 27(3):339–360. [PubMed: 8051194]

Wen D, Androjna C, Vasanji A, Belovich J, Midura RJ. Lipids and collagen matrix restrict the hydraulic permeability within the porous compartment of adult cortical bone. Ann Biomed Eng. 2010; 38(3):558–569. [PubMed: 19967451]

You L, Cowin SC, Schaffler MB, Weinbaum S. A model for strain amplification in the actin cytoskeleton of osteocytes due to fluid drag on pericellular matrix. J Biomech. 2001; 34(11): 1375–1386. [PubMed: 11672712]

You LD, Weinbaum S, Cowin SC, Schaffler MB. Ultrastructure of the osteocyte process and its pericellular matrix. Anat Rec A Discov Mol Cell Evol Biol. 2004; 278(2):505–513. [PubMed: 15164337]

Zeng Y, Cowin SC, Weinbaum S. A fiber matrix model for fluid flow and streaming potentials in the canaliculi of an osteon. Ann Biomed Eng. 1994; 22(3):280–292. [PubMed: 7978549]

Zhang D, Weinbaum S, Cowin SC. Estimates of the peak pressures in bone pore water. J Biomech Eng. 1998a; 120(6):697–703. [PubMed: 10412451]

Zhang D, Weinbaum S, Cowin SC. On the calculation of bone pore water pressure due to mechanical loading. International Journal of Solids and Structures. 1998b; 35(34–35):4981–4997.

Zhou X, Novotny JE, Wang L. Modeling fluorescence recovery after photobleaching in loaded bone: potential applications in measuring fluid and solute transport in the osteocytic lacunar-canalicular system. Ann Biomed Eng. 2008; 36(12):1961–1977. [PubMed: 18810639]

NIH-PA Author Manuscript
NIH-PA Author Manuscript
NIH-PA Author Manuscript

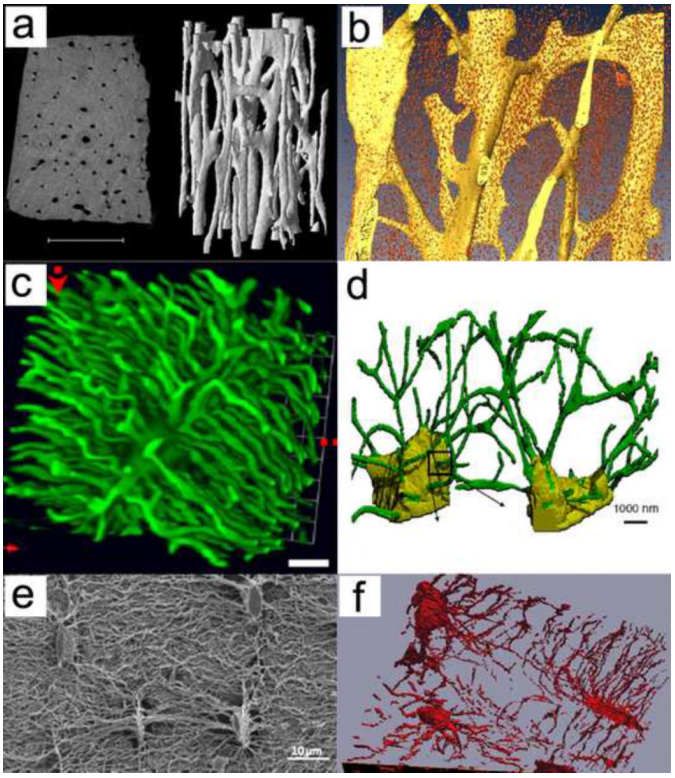

Figure 1.
Three-dimensional imaging of vascular porosity using (a) μCT (Cooper et al. 2003) and (b) SR-μCT (Hannah et al. 2010), as well as osteocyte lacunae and canaliculi using (c) confocal laser scanning microscopy (Sharma et al. 2012), (d) serial FIB/SEM (Schneider et al. 2011), (e) SEM (Kubek et al. 2010), and (f) serial FIB/SEM (Stokes et al. 2005). Reproduced with permission from Cooper et al. 2003; Hannah et al. 2010; Sharma et al. 2012; Schneider et al. 2010; Kubek et al. 2010; Stokes et al. 2005.

NIH-PA Author Manuscript

NIH-PA Author Manuscript

NIH-PA Author Manuscript

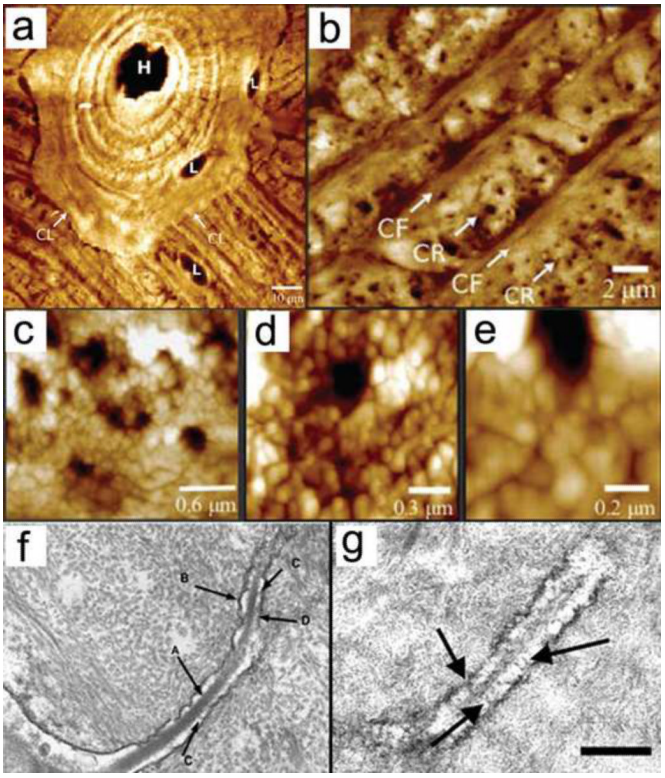

Figure 2.

Panels a-e, two-dimensional, high-resolution imaging of vascular, lacunar and canalicular pores using AFM at different magnifications (Lin and Xu 2011). Labels in panel a indicate the Haversian canal (H), lacuna (L), and cement line (CL). In panel b, canaliculi rich (CR) and canaliculi free (CF) areas are distinguished. Panel f and g display 2D high-resolution imaging of canaliculi using TEM (You et al. 2004). Panel f shows the cell process (A), canalicular wall (B), tethering elements (C), and contact beween cell process and canalicular wall (D). In panel g, tethering elements are shown with black arrows. Reproduced with permission from Lin and Xu 2011 and You et al. 2004.

NIH-PA Author Manuscript

NIH-PA Author Manuscript

NIH-PA Author Manuscript

Table 1

Imaging technologies used to characterize the vascular and lacunar-canalicular porosities.

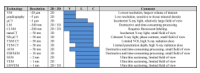

Abbreviations: Video microscopy (VM), micro-computed tomography (μCT), light microscopy (LM), confocal laser scanning microscopy (CLSM), synchrotron radiation-based micro-CT (SR-μCT), transmission X-ray microscopy CT (TXM CT), transmission electron microscopy CT (TEM CT), atomic force microscopy (AFM), focused ion beam/scanning electron microscopy (FIB/SEM), ultra-high voltage electron microscopy (UHVEM). Two-dimensional (2D), three-dimensional (3D), vascular (V), lacunar (L) and canalicular (C). Approximate imaging range capability indicated with color bar.

NIH-PA Author Manuscript
NIH-PA Author Manuscript
NIH-PA Author Manuscript

Table 2

Measurements and estimates of vascular porosity (VP), lacunar-canalicular porosity (LCP), and collagen-apatite pore (CAP) size.

Reference	Method	Tissue	Vascular Porosity (%)
Feik et al. (1997)	Digitized VM	Human femur, male	~7%
		Human femur, female	~7%
Stein et al. (1999)	Digitized VM	Human femur	5.9% (4.3 – 7.9%)
Bousson et al. (2000)	CT and microradiography	Human mid-diaphysis femur, female	~9%
		Human mid-diaphysis femur, male	~8%
Bousson et al. (2001)	Microradiography	Human mid-diaphysis femur, female	8.26 ± 0.68%
		Human mid-diaphysis femur, male	9.72 ± 0.62%
Martin-Badosa et al. (2003)	SR-μCT & LM	Mouse (B6) femur	0.8 ± 0.2%
		Mouse (C3H) femur	1.5 ± 0.3%
Cooper et al. (2004)	Microradiography & μCT	Human femur	~6%
Bousson et al. (2004)	SR-μCT	Human femoral neck	15.9 ± 9.9%
Thomas et al. (2005)	Microradiography	Human femur	4.5 – 16%
Kingsmill et al. (2007)	Backscattered SEM	Human femoral neck	16.1%
		Human mandible	3 – 11%
		Human 4th lumbar vertebrae	~5%
		Human iliac crest	~8%
Renders et al. (2007)	μCT	Human mandibular condyle	3.53 ± 1.2%
Cooper et al. (2007)	μCT	Human femur	7.29 ± 6.9%
Schneider et al. (2007)	SR-μCT	Mouse (B6) femoral mid diaphysis	1.8 ± 0.6%,
		Mouse (C3/B6) femoral mid diaphysis	4.8 ± 1.5%,
Schneider et al. (2009)	SR-μCT	Mouse (B6) femoral mid diaphysis	1.22 ± 0.26%

Reference	Method	Tissue	Lacunar-canalicular porosity (%)
Schneider et al. (2007)	SR-μCT	Mouse (B6) femoral mid-diaphysis	1.3% lacunar porosity
Tommasini et al. (2012)	SR-μCT	Rat femoral diaphysis	1.5% lacunar porosity
Schneider et al. (2011)	FIB/SEM	Mouse (B6) femoral mid-diaphysis	0.70% canalicular porosity
Sharma et al. (2012)	CLSM	Rat tibial cortical metaphysis	14% canalicular porosity (overestimated due to partial volume effects)

Reference	Tracer used	Tissue	Lacunar-canalicular and Collagen-apatite pore size
Wang et al. (2004)	Ferritin (~12 nm)	Rat tibia	Diffused through VP,
Ciani et al. (2005)		Rat tibia	but not through LCP or CAP
Knothe Tate et al. (1998)	Horseradish peroxidase (~6 nm)	Rat tibia, metacarpi	Diffused through LCP, not CAP
Dillaman et al. (1991),		Rat tibia	
Wang et al. (2004)		Rat tibia	
Knothe Tate et al. (2000)	Microperoxidase (~2 nm)	Rat tibia, metacarpi	Diffused through LCP, not CAP
Wang et al. (2004)		Rat tibia	
Knothe Tate et al. (2000)	Procion red (< 1 nm)	Rat tibia	Diffused through LCP, not CAP

Reference	Tracer used	Tissue	Lacunar-canalicular and Collagen-apatite pore size
Wang et al. (2004)	Reactive red (< 1 nm)	Rat tibia	Diffused through LCP, not CAP

NIH-PA Author Manuscript
NIH-PA Author Manuscript
NIH-PA Author Manuscript

NIH-PA Author Manuscript

NIH-PA Author Manuscript

NIH-PA Author Manuscript

Table 3

Measurements and estimates of micro/nanoarchitecture of the lacunar-canalicular network.

Reference	Method	Tissue	Lacuna per unit volume (#/mm^3)
Hannah et al. (2010)	SR-μCT	Human femur	40 – 90 (×10^3)
Tommasini et al. (2012)	SR-μCT	Rat femoral diaphysis	56.5 (×10^3)
Sharma et al. (2012)	CLSM	Rat tibial cortical metaphysis	67.3 ± 14.0 (×10^3)
Carter et al. (2012)	SR-μCT	Human femur	26 – 37 (×10^3)

Reference	Method	Tissue	Lacunar volume (μm^3)
McCreadie et al. (2004)	CLSM	Human hip	455 ± 200
Hannah et al. (2010)	SR-μCT	Human femur	290 ± 107
Sharma et al. (2012)	CLSM	Rat tibial cortical metaphysis	352 ± 30
Carter et al. (2012)	SR-μCT	Human femur	~400

Reference	Method	Tissue	Lacuna length (μm)
Vatsa et al. (2008)	CLSM	Mouse (B6) fibula,	28.7 ± 4.7
		Mouse (B6) calvaria	13.2 ± 1.5
Hannah et al. (2010)	SR-μCT	Human femur	8.96 ± 5.5
Lin and Xu (2011)	AFM	Bovine tibia, transverse direction	9.66 ± 2.82
		Bovine tibia, radial direction	10.9 ± 3.38

Reference	Method	Tissue	Lacuna width (μm)
Sugawara et al. (2005)	CLSM	Chick calvaria, E16-days-old	2 – 5
Vatsa et al. (2008)	CLSM	Mouse (B6) fibula,	7.60 ± 1.15
		Mouse (B6) calvaria	8.07 ± 0.51
Lin and Xu (2011)	AFM	Bovine tibia, transverse direction	3.86 ± 1.02
		Bovine tibia, radial direction	5.37 ± 1.71

Reference	Method	Tissue	Inter lacuna separation (μm)
Sugawara et al. (2005)	CLSM	Chick calvaria, E16-days-old	24.1 ± 2.8
Hannah et al. (2010)	SR-μCT	Human femur	21.9 ± 6.3
Sugawara et al. (2011)	CLSM	Chick calvaria, E16-days-old	23.5 ± 6.1
		Mouse calvaria (B6), E17-days-old	39.6 ± 11.6
Sharma et al. (2012)	CLSM	Rat tibial cortical metaphysis	24.8 ± 1.7

Reference	Method	Tissue	Canaliculi diameter (nm)
Marotti (1990)	SEM	Human tibia	150 – 550
You et al. (2004)	TEM	Mouse female	259 ± 129
Sugawara et al. (2005)	CLSM	Chick calvaria, E16-days-old	< 500
Lin and Xu (2011)	AFM	Bovine tibia, transverse direction	426 ± 118

NIH-PA Author Manuscript

NIH-PA Author Manuscript

NIH-PA Author Manuscript

Reference	Method	Tissue	Canaliculi diameter (nm)
		Bovine tibia, radial direction	459 ± 144
		Bovine tibia, longitudinal direction	419 ± 113
Schneider et al. (2011)	FIB/SEM	Mouse (B6) femoral mid diaphysis	95
Sharma et al. (2012)	CLSM	Rat tibia, cortical metaphysis trab. remnants	520 ± 42
		Rat tibia, cortical metaphysis lamellar region	553 ± 33
		Rat tibia, cancellous metaphysis	483 ± 24
	SEM	Rat tibia, cancellous metaphysis	335 ± 32
	TEM	Rat tibia, cancellous metaphysis	228 ± 11

Reference	Method	Tissue	Canaliculi density (#/μm^2)
Marotti et al. (1995)	SEM, light microscopy	Human tibia	0.55 ± 0.19
Lin and Xu (2011)	AFM	Bovine tibia	0.85 ± 0.31

Reference	Method	Tissue	# canaliculi per lacuna
Sugawara et al. (2005)	CLSM	Chick calvaria, E16-days-old	52.7 ± 5.7
Beno et al. (2006)	Estimated from Remaggi et al. (1998) light microscopy data	Chick	54
		Rabbit	60
		Bovine	85
		Horse	115
		Dog	81
		Human	41
Schneider et al. (2011)	FIB/SEM	Mouse (B6) femoral mid-diaphysis	78
Sugawara et al. (2011)	CLSM	Chick calvaria, E16-days-old	52.7 ± 6.4
		Mouse calvaria (B6), E17-days-old	49.7 ± 9.7
Sharma et al. (2012)	CLSM	Rat tibia, primary canaliculi	83.9 ± 14
		Rat tibia, secondary canaliculi	387 ± 34

NIH-PA Author Manuscript
NIH-PA Author Manuscript
NIH-PA Author Manuscript

Table 4

Measurements and estimates of permeability in the vascular and lacunar-canalicular systems.

Reference	Method	Tissue	VP Permeability (m^2)
Rouhana et al. (1981)	Perfusion	Bovine	3×10^{-13}
Johnson (1984)	Theoretical study	-	2.5×10^{-14}
Li et al. (1987)	Perfusion	Canine	$5\times10^{-17} – 1\times10^{-15}$
Dillaman (1984)	Theoretical study	Rat	$1\times10^{-13} – 1\times10^{-11}$
Zhang et al. (1998a)	Theoretical study	-	$1\times10^{-15} – 1\times10^{-13}$
Swan et al. (2003)	Theoretical study	-	$1.25\times10^{-13} – 3\times10^{-12}$
Malachanne et al. (2008)	Compression and FEA	Bovine, ox femurs	1.1×10^{-13}
Wen et al. (2010)	Perfusion	Canine	4×10^{-17}

Reference	Method	Tissue	LCP Permeability (m^2)
Weinbaum et al. (1994)	Ultrastructural model	-	$1\times10^{-22} – 1\times10^{-19}$
Zhang et al. (1998a)	Theoretical, adapted from Weinbaum et al. 1994	-	1.47×10^{-20}
Wang et al. (1999)	Theoretical, adapted from Weinbaum et al. 1994	-	$1.0\times10^{-21} – 1.3\times10^{-19}$
Smit et al. (2002)	Finite element analysis	-	2.20×10^{-22}
Gururaja et al. (2005)	Theoretical, adapted from Weinbaum et al. 1994	-	7.5×10^{-20}
Beno et al. (2006)	Adapted from Weinbaum et al. 1994	Chick, rabbit, bovine, horse, dog, human (data from Remaggi et al., 1998)	$1\times10^{-22} – 1\times10^{-19}$
Lemaire et al. (2008)	Glycocalyx fiber permeability, adapted from Weinbaum et al. 1994	-	$5.9\times10^{-18} – 2.0\times10^{-17}$
Anderson et al. (2008)	Perfusion on scaled-up models and predictive virtual and stochastic computational models	Scaled-up, rapid prototyped models of human femoral neck	$2.65 – 8.73\times10^{-18}$
Goulet et al. (2009)	Carman-Kozeny permeability model	-	$1.05\times10^{-18} – 1.05\times10^{-20}$
Kameo et al. (2010)	Morphology of LCP using CLSM	Swine tibia	$3.3\times10^{-19} – 1.27\times10^{-18}$
Lemaire et al. (2012)	FEM, Carman-Kozeny permeability model	-	$1\times10^{-19} – 1\times10^{-18}$
Oyen (2008)	Nanoindentation-poroelasticity	Human	4.14×10^{-24}
Galli and Oyen (2009)	Nanoindentation-poroelasticity	Human	6.5×10^{-23}
Zhou et al. (2008)	FRAP-poroelasticity	Mice	$\sim10^{-21}$
Gailani et al. (2009)	Stress relaxation single osteons-poroelasticity	Bovine	$5\times10^{-25} – 8\times10^{-24}$
Gardinier et al. (2010)	Step loading *in vivo*-poroelasticity	Canine	2.8×10^{-23}